

Theory of Josephson Arrays in a Resonant Cavity

E. Almaas*

Department of Physics, University of Notre Dame, Notre Dame, Indiana 46556

D. Stroud†

Department of Physics, The Ohio State University, Columbus, Ohio 43210

(Dated: February 8, 2020)

We review our previous work on the dynamics of one- and two-dimensional arrays of underdamped Josephson junctions placed in a single-mode resonant cavity. Starting from a well-defined model Hamiltonian, which includes the effects of driving current and dissipative coupling to a heat bath, we write down the Heisenberg equations of motion for the variables of the Josephson junction and the cavity mode. In the limit of many photons, these equations reduce to coupled ordinary differential equations, which can be solved numerically. We present a review of some characteristic numerical results, which show many features similar to experiment. These include self-induced resonant steps (SIRS's) at voltages $V = n\hbar\Omega/(2e)$, where Ω is the cavity frequency, and n is generally an integer; a threshold number N_c of active rows of junctions above which the array is coherent; and a time-averaged cavity energy which is quadratic in the number of active junctions, when the array is above threshold. When the array is biased on a SIRS, then, for given junction parameters, the power radiated into the array varies as the square of the number of active junctions, consistent with expectations for coherent radiation. For a given step, a two-dimensional array radiates much more energy into the cavity than does a one-dimensional array. Finally, in two dimensions, we find a strong polarization effect: if the cavity mode is polarized perpendicular to the direction of current injection in a square array, then it does not couple to the array and no power is radiated into the cavity. In the presence of an applied magnetic field, however, a mode with this polarization would couple to an applied current. We speculate that this effect might thus produce SIRS's which would be absent with no applied magnetic field.

PACS numbers: 05.45.Xt, 79.50.+r, 05.45.-a, 74.40.+k

I. INTRODUCTION

The properties of arrays of Josephson junctions have been of great interest for nearly twenty years.¹ These arrays are excellent model systems in which to study phenomena such as phase transitions and quantum coherence in two dimensions. For example, if only the Josephson coupling energy is considered, and if the self-inductance and mutual inductance of the array plaquettes are neglected, the Hamiltonian of a two-dimensional (2D) array of Josephson junctions is formally identical to that of a 2D XY model [see, e. g. Ref. 2]. In the presence of such inductive effects, this XY description needs to be modified, and several generalizations, which include these effects, have been proposed.^{3,4,5,6} Arrays sometimes appear to mimic behavior seen in nominally homogeneous materials, e. g. high- T_c superconductors, which often behave as if they are composed of distinct superconducting regions linked together by Josephson coupling.⁷ Finally, the arrays are of potentially practical interest: they may be useful, for example, as sources of coherent microwave radiation if the individual junctions can be caused to oscillate in phase in a stable manner.

Recently, our ability to achieve this kind of stable oscillation, and coherent microwave radiation, was significantly advanced by a series of experiments by Barbara and collaborators.^{8,9,10,11,12} These workers placed two-dimensional underdamped Josephson arrays in a resonant microwave cavity. The presence of the cavity caused the junctions to couple together with remarkable efficiency, resulting in a highly efficient conversion of the injected d. c. power into a. c. radiation. Even more surprising, this efficiency is achieved in *underdamped* arrays, which according to conventional wisdom, should be especially difficult to synchronize, since each such junction is both bistable and hysteretic. Numerous workers have attempted to explain these experiments.^{13,14,15,16}

In this brief review, we summarize our own model to describe this kind of phase locking.^{16,17} In Section II, we present the model Hamiltonian. In Section III, we describe the equations of motion resulting from this model, in the “classical limit,” as defined further below. In Section IV, we give a brief description of the relevant numerical results. Finally, in Section V, we present a concluding discussion.

II. MODEL HAMILTONIAN

We consider a 2D array of $N \times M$ superconducting grains placed in a resonant cavity, which we assume supports only a single photon mode of frequency Ω . The array thus has $(N-1)(M-1)$ square plaquettes. There are a total of $N_x \times N_y$ horizontal junctions, where $N_x = N-1$ and $N_y = M$. A current I is fed into each of the M grains on the left edge of the array, and extracted from each of the M grains on the right edge. Thus, the current is injected in the x direction, with no external current injected in the y direction. A sketch of this geometry is shown in Fig. 1. We also introduce the terminology that a “row” of junctions, in this configuration, refers to a group of N_y junctions, all with left-hand end having the same x coordinate, and all being parallel to the bias current. One such row is indicated by the dashed lines in Fig. 1.

We write the equations of motion for the grain variables (phases and charges). We express our Hamiltonian in the form:^{16,17}

$$H = H_{\text{photon}} + H_J + H_C + H_{\text{curr}} + H_{\text{diss}}. \quad (1)$$

Here H_{photon} is the energy of the cavity mode, expressed as

$$H_{\text{photon}} = \hbar\Omega \left(a^\dagger a + \frac{1}{2} \right), \quad (2)$$

where a^\dagger and a as the usual photon creation and annihilation operators. H_J is the Josephson coupling energy, which takes the form

$$H_J = - \sum_{\langle ij \rangle} E_{ij}^J \cos(\gamma_{ij}), \quad (3)$$

where E_{ij}^J is the Josephson energy of the $(ij)^{\text{th}}$ junction, and γ_{ij} is the gauge-invariant phase difference across that junction. E_{ij}^J is related to I_{ij}^c , the critical current of the $(ij)^{\text{th}}$ junction, by $E_{ij}^J = \hbar I_{ij}^c / q$, where $q = 2|e|$ is the Cooper pair charge. H_C is the capacitive energy of the array, which we write as

$$H_C = \frac{1}{2} \sum_{ij} q^2 (C^{-1})_{ij} n_i n_j, \quad (4)$$

where C^{-1} is the inverse capacitance matrix, n_i is the number of Cooper pairs on the i^{th} grain, and $q = 2e$ is the charge of a Cooper pair (we take $e > 0$). We write γ_{ij} as

$$\gamma_{ij} = \phi_i - \phi_j - [(2\pi)/\Phi_0] \int_{ij} \mathbf{A} \cdot d\mathbf{s} \equiv \phi_i - \phi_j - A_{ij}, \quad (5)$$

where ϕ_i is the gauge-dependent phase of the superconducting order parameter on grain i , $\Phi_0 = hc/(2e)$ is the flux quantum, and \mathbf{A} is the vector potential, which in Gaussian units takes the form^{18,19}

$$\mathbf{A}(\mathbf{x}, t) = \sqrt{(\hbar c^2)/(\Omega)} (a(t) + a^\dagger(t)) \mathbf{E}(\mathbf{x}), \quad (6)$$

where $\mathbf{E}(\mathbf{x})$ is a vector proportional to the local electric field of the mode, normalized such that $\int_V d^3x |\mathbf{E}(\mathbf{x})|^2 = 1$. Again, Ω is the resonant frequency of the cavity mode, and V is the cavity volume. The line integral is taken across the $(ij)^{\text{th}}$ junction. The phase factor A_{ij} is then

$$A_{ij} = g_{ij}(a + a^\dagger), \quad (7)$$

where

$$g_{ij} = \sqrt{\frac{\hbar c^2}{\Omega} \frac{(2\pi)^3}{\Phi_0^2}} \int_{ij} \mathbf{E} \cdot d\mathbf{s} \quad (8)$$

characterizes the effective coupling between the $(ij)^{\text{th}}$ junction and the cavity.

One can also define a *frustration* f_μ for the μ^{th} plaquette by the relation

$$f_\mu = \frac{1}{2\pi} \sum_{\text{plaquette}} A_{ij}, \quad (9)$$

where the sum runs over the bonds in the μ^{th} plaquette. For the present case,

$$f_\mu = f_\mu^{cavity} = \frac{1}{2\pi}(a + a^\dagger) \sum_{\text{plaquette}} g_{ij}. \quad (10)$$

If there were an applied magnetic field normal to the array in addition to the cavity electric field, then the frustration would have an additional contribution

$$f_\mu^{mag} = \Phi_\mu / \Phi_0, \quad (11)$$

where Φ_μ is the magnetic flux through the μ^{th} plaquette.²⁰

Note that g_{ij} is very sensitive to the experimental geometry. For example, if the cavity has the form of a parallelepiped with edges L_x , L_y , and L_z , where $L_z \geq L_x \geq L_y$, then lowest mode in this cavity is a TE mode with frequency $\Omega = \pi c \sqrt{1/L_z^2 + 1/L_y^2}$; the corresponding value of g_{ij} is given by¹⁷

$$g_{ij}^2 = e_{ij}^2 \frac{32e^2}{\hbar c} \frac{s^2}{L_y \sqrt{L_x^2 + L_z^2}}, \quad (12)$$

where e_{ij} is the cosine of the angle between the \mathbf{E} of the resonant mode and the vector \mathbf{ds} . In the geometry of Ref. 8, $\Omega/(2\pi) \approx 100$ GHz, a cavity of this shape gives rise to $g_{ij} \sim 0.001$,¹⁷ though it is obviously very sensitive to both array and cavity geometry.

The driving current and dissipation may be incorporated as follows:^{16,17} The driving current is included via a “washboard potential,” H_{curr} , of the form

$$H_{curr} = -\frac{\hbar I^{ext}}{q} \sum_{\langle ij \rangle \parallel \hat{\mathbf{x}}} \gamma_{ij}, \quad (13)$$

where I is the driving current injected in the x direction into *each* grain on the left edge and extracted from the right edge, the sum running over bonds in the x direction. Dissipation is included by coupling each γ_{ij} to a separate collection of harmonic oscillators with a suitable spectral density.^{21,22,23,24}

$$H_{diss} = \sum_{\langle ij \rangle} H_{ij}^{diss}, \quad (14)$$

where the sum runs over distinct bonds $\langle ij \rangle$, and

$$\begin{aligned} H_{ij}^{diss} = & \sum_{\alpha} \left[f_{\alpha,ij} \gamma_{ij} u_{\alpha,ij} + \frac{(p_{\alpha,ij})^2}{2m_{\alpha,ij}} \right. \\ & \left. + \frac{1}{2} m_{\alpha,ij} (\omega_{\alpha,ij})^2 (u_{\alpha,ij})^2 + \frac{(f_{\alpha,ij})^2}{2 m_{\alpha,ij} (\omega_{\alpha,ij})^2} (\gamma_{ij})^2 \right]. \end{aligned} \quad (15)$$

The variables $u_{\alpha,ij}$ and $p_{\alpha,ij}$ of the α^{th} oscillator in the $(ij)^{th}$ junction, are canonically conjugate, and $m_{\alpha,ij}$ and $\omega_{\alpha,ij}$ are the oscillator mass and frequency. If the spectral density, $J_{ij}(\omega) \propto |\omega|$, the dissipation is ohmic.^{22,23} We write such a linear spectral density as

$$J_{ij}(\omega) = \frac{\hbar}{2\pi} \alpha_{ij} |\omega| \Theta(\omega_c - \omega), \quad (16)$$

where ω_c is a high-frequency cutoff, $\Theta(\omega_c - \omega)$ is a step function, and the dimensionless constant $\alpha_{ij} = R_0/R_{ij}$, where $R_0 = \hbar/(4e^2)$ and R_{ij} is a constant with dimensions of resistance, which turns out to be the effective shunt resistance.

III. EQUATIONS OF MOTION

The equations of motion are obtained by introducing operators $a = a_R + ia_I$ and $a^\dagger = a_R - ia_I$. These satisfy the commutation relation $[a_R, a_I] = i/2$, which follows from $[a, a^\dagger] = 1$. In terms of these variables, $H_{photon} = \hbar\Omega(a_R^2 + a_I^2)$ and $\gamma_{ij} = \phi_i - \phi_j - 2g_{ij}a_R$.

The time-dependence of the various operators appearing in the Hamiltonian (1) is now obtained from the Heisenberg equations of motion. These are readily derived from the commutation relations for the various operators in the Hamiltonian (1). Besides the relations already given, the only non-zero commutators are $[n_j, \phi_k] = -i\delta_{jk}$ and $[p_{\alpha,ij}, u_{\beta,k\ell}] = -i\hbar \delta_{\alpha,\beta} \delta_{ij,k\ell}$, where the last delta function vanishes unless (ij) and $(k\ell)$ refer to the *same* junction.

Using all these relations, we find, after a little algebra, the following equations of motion for the operators ϕ_i , n_i , a_R , and a_I :

$$\dot{\phi}_i = \frac{q^2}{\hbar} \sum_j (C^{-1})_{ij} n_j, \quad (17)$$

$$\begin{aligned} \dot{n}_i = & -\frac{1}{\hbar} \sum_l E_{il}^J \sin(\phi_i - \phi_l - 2g_{il}a_R) \\ & + \frac{I_i^{ext}}{q} - \frac{1}{\hbar} \sum_l \sum_{\alpha} \left[u_{\alpha,il} f_{\alpha,il} + \frac{(f_{\alpha,il})^2}{m_{\alpha,il}(\omega_{\alpha,il})^2} (\phi_i - \phi_l - 2g_{il}a_R) \right], \end{aligned} \quad (18)$$

$$\dot{a}_R = \Omega a_I, \quad (19)$$

$$\begin{aligned} \dot{a}_I = & -\Omega a_R + \sum_{\langle ij \rangle} g_{ij} \frac{E_{ij}^J}{\hbar} \sin(\phi_i - \phi_j - 2g_{ij}a_R) - \frac{I^{ext}}{q} \sum_{\langle ij \rangle \parallel \hat{x}} g_{ij} \\ & + \sum_{\langle ij \rangle} \frac{g_{ij}}{\hbar} \sum_{\alpha} \left(f_{\alpha,ij} u_{\alpha,ij} + \frac{(f_{\alpha,ij})^2}{m_{\alpha,ij}\omega_{\alpha,ij}^2} (\phi_i - \phi_j - 2g_{ij}a_R) \right). \end{aligned} \quad (20)$$

Here, the index l ranges over the nearest-neighbor grains of i . In writing these equations, we have assumed that the only external currents I_i^{ext} are those along the left and right edges of the array, where they are $\pm I^{ext}$ [cf. Fig. 1]. Eqs. (17)-(20) are equations of motion for the *operators* a_R , a_I , n_j , and ϕ_j (or γ_j). In order to make these equations amenable to computation, we will regard these operators as *c*-numbers. This should be reasonable when there are many photons in the cavity.^{16,17}

The equations of motion for the harmonic oscillator variables can also be written out explicitly, but are of no interest; we instead eliminate those variables and incorporate a dissipative term directly into the equations of motion for the other variables. Such a replacement is possible provided that the spectral density of each junction is linear in frequency, as above. In that case,^{16,21,22,23,24} the oscillator variables can be integrated out. The effect of carrying out this procedure is that one should make the replacement $\sum_{\alpha} \left(f_{\alpha,ij} u_{\alpha,ij} + \frac{(f_{\alpha,ij})^2}{m_{\alpha,ij}\omega_{\alpha,ij}^2} \gamma_{ij} \right) \rightarrow \frac{\hbar}{2\pi} \frac{R_0}{R_{ij}} \dot{\gamma}_{ij}$ wherever this sum appears in the equations of motion. Making this replacement in the equations of motion and simplifying, we obtain the equations of motion for n_j and a_I with damping:

$$\dot{n}_i = -\sum_j \frac{E_{ij}^J}{\hbar} \sin(\gamma_{ij}) + \frac{I_i^{ext}}{q} - \sum_j \frac{1}{2\pi} \frac{R_0}{R_{ij}} \dot{\gamma}_{ij}, \quad (21)$$

$$\dot{a}_I = -\Omega a_R + \sum_{\langle ij \rangle} g_{ij} \frac{E_{ij}^J}{\hbar} \sin(\gamma_{ij}) - \frac{I^{ext}}{q} \sum_{\langle ij \rangle \parallel \hat{x}} g_{ij} + \sum_{\langle ij \rangle} g_{ij} \frac{R_0}{2\pi R_{ij}} \dot{\gamma}_{ij}. \quad (22)$$

Once, again, the index j is summed only over the nearest-neighbor grains of i . Equations (17), (19), (21), and (22) form a closed set of equations which can be solved for the time-dependent functions γ_i , n_i , a_R and a_I , given the external current and the other parameters.

To express these equations of motion in terms of suitable scaled variables, we introduce a dimensionless time $\tau = tqRI^c/\hbar = \omega_{\tau}t$, where R and I^c are suitable averages over R_{ij} and I_{ij}^c . We also define the other scaled variables $\tilde{R}_{ij} = \frac{R_{ij}}{R}$, $\tilde{\Omega} = \frac{\Omega}{\omega_{\tau}}$, $\tilde{I} = \frac{I}{I^c}$, $\tilde{V}_i = \frac{V_i}{RI^c}$, $\tilde{a}_{R,I} = \sqrt{2\pi \frac{R}{R_0}} a_{R,I}$, $\tilde{g}_{ij} = \sqrt{\frac{R_0}{2\pi R}} g_{ij}$, $\tilde{C}_{ij} = \omega_{\tau} R C_{ij}$. The last relation involves the capacitance matrix C_{ij} . We assume that this takes the form^{25,26} $C_{ij} = (C_d + z_i C_c) \delta_{ij} - C_c (\delta_{i,j+\hat{x}} + \delta_{i,j-\hat{x}} + \delta_{i,j+\hat{y}} + \delta_{i,j-\hat{y}})$, i. e., that there is a non-vanishing capacitance only between neighboring grains and between a grain and ground. Here $z_i (= 4)$ is the number of nearest neighbors of grain i , C_d and C_c are respectively the diagonal (self) and nearest-neighbor capacitances, and \hat{x} and \hat{y} are unit vectors in the x and y directions. The corresponding Stewart-McCumber parameters are $\beta_c = \omega_{\tau} R C_c$ and $\beta_d = \omega_{\tau} R C_d$.

In the above equations, we have introduced $V_i = q \sum_j (C^{-1})_{ij} n_j$, which is the potential on site i . The integral of the electric field across junction (ij) is $V_{ij} = V_i - V_j - 2\tilde{g}_{ij}\Omega a_I$.

Carrying out these variable changes, and after some algebra, we find the dimensionless equations of motion

$$\dot{\phi}_i = \tilde{V}_i, \quad (23)$$

$$\dot{V}_i = \sum_j (\tilde{C}^{-1})_{ij} \left[\tilde{I}_j^{ext} - \sum_l \left(\tilde{I}_{jl}^c \sin(\phi_j - \phi_l - 2\tilde{g}_{jl}a_R) + \frac{1}{\tilde{R}_{jl}} (\tilde{V}_i - \tilde{V}_l - 2\tilde{g}_{il}\tilde{\Omega}\tilde{a}_I) \right) \right], \quad (24)$$

$$\dot{\tilde{a}}_R = \tilde{\Omega}\tilde{a}_I, \quad (25)$$

and

$$\dot{\tilde{a}}_I = -\tilde{\Omega}\tilde{a}_R + \sum_{\langle ij \rangle} \tilde{g}_{ij} \left[\tilde{I}_{ij}^c \sin(\phi_i - \phi_j - 2\tilde{g}_{ij}\tilde{a}_R) + \frac{1}{\tilde{R}_{ij}} (\tilde{V}_i - \tilde{V}_j - 2\tilde{\Omega}\tilde{g}_{ij}\tilde{a}_I) \right] - \tilde{I}^{ext} \sum_{\langle ij \rangle \parallel \hat{x}} \tilde{g}_{ij}, \quad (26)$$

where the dot refers to a derivative with respect to τ . These equations do not include the self-magnetic fields produced by the currents.^{3,4,5,6} However, they can be generalized to include external currents with both x and y components, and non-square primitive cells. Also, note that the frustration parameter defined earlier is now time-dependent.

IV. SOME NUMERICAL RESULTS

We now describe some numerical results obtained by solving Eqs. (23) - (26) numerically,¹⁷ using the adaptive Bulirsch-Stoer method²⁷ as further described in Ref. 16. For simplicity the coupling constants \tilde{g}_{ij} were assumed to have only two possible values, \tilde{g}_x and \tilde{g}_y , corresponding to junctions in the x and y direction respectively. This assumption should be reasonable if there is little disorder and the resonant mode has long wavelength compared to the array dimensions.

The calculated IV characteristics for the case $\tilde{g}_x \neq 0$, $\tilde{g}_y = 0$, with driving current parallel to the x axis are shown in Fig. 2. The array is taken to have 10×4 grains, with capacitances $\beta_c = 20$ and $\beta_d = 0.05$ (independent of junction), $\tilde{g}_x = 0.012$, and $\tilde{\Omega} = 0.41$. The critical current through the $(ij)^{th}$ junction is $\tilde{I}_{ij}^c = 1 + \Delta_{ij}$ where the disorder Δ_{ij} is randomly selected with uniform probability from $[-\Delta, \Delta]$, and $\Delta = 0.05$. The product $\tilde{I}_{ij}^c \tilde{R}_{ij}$ is assumed to be the same for all junctions, in accordance with the Ambegaokar-Baratoff expression.²⁸ The calculated IV's are shown as a series of points. The arrow directions of the arrows indicate whether the curves were obtained under increasing or decreasing current drive, or both. The horizontal dashed curves are voltages where *self-induced resonant steps* (SIRS's) are expected, namely $\langle V \rangle_\tau / (NRI_c) = \tilde{\Omega}$, where $\langle V \rangle_\tau$ is the time-averaged voltage (dotted lines are guides to the eye). Each nearly horizontal series of points denotes a calculated IV characteristic for a *different* number of active rows N_a , and represents $N_a \times N_y$ (horizontal) junctions sitting on the first integer ($n = 1$) SIRS. The calculated voltages agree well with expected values given by dashed horizontal lines. The long straight diagonal line segment represents the ohmic part of the IV characteristic with all rows active. (The corresponding segments for other choices of $N_a < 10$ are not shown). Besides the integer SIRS's, there are a few fractional SIRS's, similar to what is seen for Shapiro steps in conventional underdamped junctions.²⁹

Fig. 3 shows the IV characteristics for three different arrays, each with all rows in the active state: (i) a 40×1 (full curve), (ii) a 40×2 (dotted curve) and (iii) a 40×3 (long-dashed curve). Each array has the parameters $\tilde{g}_x = 0.015$, $\tilde{\Omega} = 0.49$, $\beta_c = 20$, $\beta_d = 0.05$ and $\Delta = 0.05$. Once again, the arrows denote the directions of current sweep. The horizontal dot-dashed curve shows the expected position of the SIRS corresponding to $N_a = 40$ [$V/(N_x RI_c) = \tilde{\Omega}$]. The curves show that all three arrays have qualitatively similar behavior. First, if the array is started from a random initial phase configuration, such that $\tilde{I} \equiv I/I_c > 1 + \Delta$, and \tilde{I} is decreased, then all the rows lock on to the $N_a = 40$ SIRS. Secondly, if \tilde{I} is further decreased, the $N_a = 40$ active state eventually becomes unstable and all the junctions go into their superconducting states. Finally, if \tilde{I} is *increased* starting from a state in which the array is on the $N_a = 40$ SIRS, the SIRS remains stable until \tilde{I} reaches the critical current for the various rows, and the IV curve becomes ohmic.

In Fig. 4, we plot the time-averaged energy $\tilde{E}(N_a) = \langle \tilde{a}_R^2 + \tilde{a}_I^2 \rangle_\tau$ in the cavity for three different arrays: 40×1 (stars), 40×2 (circles), and 40×3 (squares). In all cases, $\tilde{I} = 0.58$, and the other parameters are the same as those of Fig. 3. Below a threshold value of N_a , (which we denote N_c and which depends on N_y), the active rows are in the McCumber state (not on the SIRS's). In this case, $\tilde{E}(N_a)$ is small and shows no obvious functional dependence on N_a (see inset). By contrast, above threshold, $\tilde{E}(N_a)$ is much larger and increases as N_a^2 . Fig. 4 shows that, when N_y is increased at fixed \tilde{g}_x , N_c decreases. Precisely this same trend is observed when we increase \tilde{g}_x while holding N_y fixed (and was observed in our previous 1D calculations with increasing \tilde{g}_x). Thus, the relevant parameter in understanding the threshold behavior appears to be $N_y \tilde{g}_x$.

For the 2D arrays, one can introduce a define a *Kuramoto order parameter* $\langle r_h \rangle_\tau$ for the horizontal bonds by

$$\langle r_h \rangle_\tau = \frac{1}{N_a N_y} \langle | \sum_{\langle ij \rangle \parallel \mathbf{x}} e^{i\gamma_{ij}} | \rangle_\tau, \quad (27)$$

where N_a is the number of active rows, N_y is the number of horizontal junctions in a single row and the sum runs over all the active, horizontal junctions. For the parameters shown in Fig. 4, it is found,¹⁷ as in 1D,¹⁶ that $\langle r_h \rangle_\tau \sim 1$ for $N_a > N_c$ while $\langle r_h \rangle_\tau \ll 1$ for $N_a < N_c$. This behavior occurs because, for this choice of parameters, none of the active junctions are on a SIRS when $N_a < N_c$.

For the case $\tilde{g}_x = 0$, $\tilde{g}_y \neq 0$, in our geometry (with square primitive cells), we have not been able to find *any* value for \tilde{g}_y for which a SIRS develops. This behavior is easily understood. In this geometry, with current applied in the x direction, there is little power dissipated in the vertical junctions and no resonance is induced in the cavity.

It is no surprise that the cavity interacts only very weakly with the vertical junctions. From previous studies of both underdamped and overdamped disordered Josephson arrays in a rectangular geometry (see, e. g., Refs. 30, and 31), it is known that when current is applied in the x direction, the y junctions remain superconducting, with $\langle V \rangle_\tau \approx 0$, while the x junctions comprising an active row are almost perfectly synchronized, with $\langle r_x \rangle \approx 1$.

If there were an external magnetic field *perpendicular* to the array, we believe that SIRS's would be generated for $\tilde{g}_y \neq 0$, even if $\tilde{g}_x = 0$. In this case, as mentioned earlier, there would be a non-zero magnetic-field-induced frustration f_μ^{mag} [Eq. (11)]. As a result of this magnetic-field-induced frustration, there would be nonzero voltages across the y junctions, as well as supercurrents in these junctions.

It is of interest to compare these 2D results explicitly with those of 1D arrays. In Fig. 5, the IV characteristics of a 10×1 array having coupling constant $\tilde{g}_{x;10 \times 1} = 0.0259$ with those of a 10×10 array with coupling constant $\tilde{g}_{x;10 \times 10} = 0.00259$. The other parameters are the same for the two arrays: $\tilde{\Omega} = 0.41$, $\beta_c = 20$, $\beta_d = 0.05$ and $\Delta = 0.05$. The expected positions of the SIRS's [at $V/(NRI_c) = \tilde{\Omega}$] are indicated by dashed horizontal lines. Indeed, the two sets of IV characteristics are very similar. This indicates that the crucial parameter is $N_y \tilde{g}_x$, not N_y and \tilde{g}_x independently. The slight extra flatness in the 10×10 IV's probably occurs because the individual junction couplings in the 10×1 array are 10 times larger than those in the 10×10 array. Similarly, the differences in the “retrapping current” in the two sets of curves (i. e. the current values below which the McCumber curve becomes unstable), are due to the fact that, for a given value of Δ , the 2D arrays are effectively less disordered than the 1D arrays, since the *average* critical current for a single row has a smaller rms spread than the critical current of a single junction in a 1D array. (For other discussions of the effects of disorder, see, e. g., Refs. 32,33,34).

In both the 10×10 and the 10×1 array of Fig. 5, the width of the SIRS's varies similarly (and non-monotonically) with the number of active rows. This behavior distinguishes our predictions from those of some other models,^{13,14} where a monotonic dependence of SIRS width on N_a is found,⁹ and the cavity is modeled as an RLC oscillator connected in parallel to the entire array.

In Fig. 6, the reduced time-averaged cavity energy $\tilde{E} = \langle a_R^2 + a_I^2 \rangle_\tau$ is plotted vs. $\tilde{I} = I/I_c$ for both arrays of Fig. 5, under conditions such that all rows are active. This plot is obtained by following the decreasing current branch. When the 10×10 array (with $\tilde{g}_{(10 \times 10)} = 0.1 \tilde{g}_{(10 \times 1)}$) locks on to the SIRS, \tilde{E} jumps to a value which is approximately two orders of magnitude *larger* than in the 10×1 array, even though $N_y \tilde{g}_x$ is the same for both arrays. The reason is that though the *width* of the steps is controlled primarily by $N_y \tilde{g}_x$, the energy in the cavity is determined by the *square* of the number of radiating junctions, which is *100 times larger* for the 2D than the 1D array.

V. DISCUSSION AND SUMMARY

The equations of motion described lead to a transition from incoherence to coherence, as a function of the number of active rows N_a . There is also a striking effect of polarization: the transition to coherence occurs only when the cavity mode is polarized so that its electric field has a component parallel to the direction of the current flow.

The numerical results closely resemble the experimental behavior,^{8,11} showing the following experimental features: (i) self-induced resonant steps (SIRS's) in the IV characteristics; (ii) a transition from incoherence to coherence above a threshold number of active junctions; and (iii) a total energy in the cavity which varies quadratically with the number of active junctions when those junctions are locked onto SIRS's. But there may be some differences, as discussed further in Ref. 17.

The 2D theory bears many similarities to the 1D case and elucidates why the 1D model works so well. These similarities occur because, in a square array, only junctions which are *parallel* to the applied current couple to the cavity. Thus, as in 1D, the 2D model leads to clearly defined SIRS's with voltages proportional to the cavity resonant frequency. However, there are some numerical results specific to 2D. For example, whenever one junction in a given

row is biased on a SIRS, *all* the junctions in that row phase-lock onto that same SIRS. In addition, when the array is biased on a SIRS, $\bar{E}(N_a)$ is much *larger* in 2D than in 1D, for the same value of the coupling parameter $\tilde{g}_x N_y$.

A key difference between 1D and 2D is the effect of polarization: when the cavity mode is polarized perpendicular to the applied current, it does not affect the array IV characteristics. We believe that, if the array were frustrated, e. g. by an external magnetic field normal to the plane of the array, there would be a coupling even when the cavity mode is polarized perpendicular to the current. It would be of interest to carry out calculations for the model described here, to confirm this effect.

We conclude with a brief discussion of ways in which our model might be generalized to include some effects which are presently not taken into account. First, of course, one should include the fact that the cavity, as well as the junctions, has a finite damping (finite Q). Second, the real cavity fields are not spatially uniform within the array, as assumed in the calculations presented here. We speculate that the effect of these two generalizations would be to inhibit the array synchronization. Third, all real cavities have more than one resonant mode; these other modes may be relevant in some experimental circumstances. Fourth, we have treated the operators as c -numbers, i. e., have neglected quantum effects related to their non-commutativity. These quantum effects will certainly be relevant in some circumstances. Finally, the present treatment of damping within individual Josephson junctions is also carried out in the classical limit (resistively and capacitively shunted Josephson junction); in the quantum regime where the individual junction variables need to be treated quantum-mechanically, this treatment will need to be modified.

Most of these generalizations can probably be carried out in a straightforward manner. Thus, we believe that the present model has most of the essential physics underlying the SIRS's seen in experiments. Of the omitted effects, we believe that the quantum effects, if included, are most likely to produce qualitative changes, because they could lead to intriguing entanglement between quantum states of the array and of the cavity.³⁵

VI. ACKNOWLEDGMENTS

This work has been supported by the National Science Foundation, through grant DMR01-04987, and in part by the U.S.-Israel Binational Science Foundation. Some of the calculations were carried out using the facilities of the Ohio Supercomputer Center, with the help of a grant of time. We are very grateful for valuable conversations with Profs. T. R. Lemberger and C. J. Lobb.

-
- * Electronic address: Almaas.1@nd.edu
† Electronic address: stroud@mps.ohio-state.edu
- ¹ For an extensive review, see, e. g. R. S. Newrock, C. J. Lobb, U. Geigenmüller, and M. Octavio, *Solid State Physics* **54**, 263 (2000).
 - ² See, for example, P. M. Chaikin and T. C. Lubensky. *Principles of Condensed Matter Physics*. Cambridge Univ. Press, New York, 1995.
 - ³ K. Nakajima and Y. Sawada. *J. Appl. Phys.* **52**, 5732 (1981).
 - ⁴ A. Majhofer, T. Wolf, and W. Dieterich. *Phys. Rev. B* **44**, 9634 (1991).
 - ⁵ J. R. Phillips, H. S. J. Van der Zant, J. White, and T. P. Orlando. *Phys. Rev. B* **47**, 5219 (1993).
 - ⁶ A. Petraglia, G. Filatrella, and G. Rotoli, *Phys. Rev. B* **53**, 2732 (1996).
 - ⁷ M. Tinkham. *Introduction to Superconductivity*. McGraw-Hill, New York, Second edition, 1996.
 - ⁸ P. Barbara, A. B. Cawthorne, S. V. Shitov, and C. J. Lobb. *Phys. Rev. Lett.* **82**, 1963 (1999).
 - ⁹ P. Barbara, G. Filatrella, C. J. Lobb, and N. F. Pedersen, "Cavity Synchronization of Underdamped Josephson-Junction Arrays." In A. Narlikar, editor, *Studies in High-Temperature Superconductors*, volume 40, 185. Nova Science Publishers, New York, 2002.
 - ¹⁰ B. Vasilic, P. Barbara, S. V. Shitov, and C. J. Lobb. *IEEE Trans. Appl. Superconductivity* **11**, 1188 (2001).
 - ¹¹ B. Vasilic, P. Barbara, S. V. Shitov, and C. J. Lobb. *Phys. Rev. B* **65**, 180503(R) (2002).
 - ¹² B. Vasilic, P. Barbara, S. V. Shitov, E. Ott, T. M. Antonsen, and C. J. Lobb, *Bull. Am. Phys. Soc.* **46**, Abstract Y27.001 (2001).
 - ¹³ G. Filatrella, N. F. Pedersen, and K. Wiesenfeld. *Phys. Rev. E* **61**, 2513 (2000).
 - ¹⁴ G. Filatrella, N. F. Pedersen, and K. Wiesenfeld. *IEEE Trans. Appl. Supercond.*
 - ¹⁵ E. Almaas and D. Stroud. *Phys. Rev. B* **63**, 144522 (2001). See also E. Almaas and D. Stroud, *Phys. Rev. B* **64**, 179902(E) (2001).
 - ¹⁶ E. Almaas and D. Stroud. *Phys. Rev. B* **65**, 134502 (2002).
 - ¹⁷ E. Almaas and D. Stroud, *Phys. Rev. B* **67**, 064511 (2003).
 - ¹⁸ J. C. Slater. *Microwave Electronics*. D. Van Nostrand, New York, 1950.
 - ¹⁹ A. Yariv. *Quantum Electronics*. J. Wiley & Sons, New York, Second edition, 1975.
 - ²⁰ See, for example, S. Teitel and C. Jayaprakash. *Phys. Rev. B* **27**, 598 (1983).

- ²¹ V. Ambegaokar, U. Eckern, and G. Schön. Phys. Rev. Lett. **48**, 1745 (1982).
- ²² A. O. Caldeira and A. J. Leggett. Phys. Rev. Lett. **46**, 211 (1981).
- ²³ A. O. Caldeira and A. J. Leggett. Ann. Phys. (N. Y.) **149**, 374 (1983).
- ²⁴ S. Chakravarty, G.-L. Ingold, S. Kivelson, and A. Luther. Phys. Rev. Lett. **56**, 2303 (1986).
- ²⁵ R. Fazio and G. Schön. Phys. Rev. B **43**, 5307 (1990).
- ²⁶ B. J. Kim and M. Y. Choi. Phys. Rev. B **52**, 3624 (1995).
- ²⁷ W. H. Press, S. A. Teukolsky, W. T. Vetterling, and B. P. Flannery. *Numerical Recipes*. Cambridge Univ. Press, New York, 1992.
- ²⁸ V. Ambegaokar and A. Baratoff. Phys. Rev. Lett. **10**, 486 (1963).
- ²⁹ J. R. Waldram. *Superconductivity of Metals and Cuprates*. Inst. of Phys. Publ., Philadelphia, 1996.
- ³⁰ W. Yu and D. Stroud. Phys. Rev. B **46**, 14005 (1992).
- ³¹ W. Yu. *Topics in the Dynamical Properties of Josephson Networks*. PhD thesis, The Ohio State University, 1994.
- ³² M. Octavio, C. B. Whan, and C. J. Lobb. Appl. Phys. Lett. **60**, 766 (1992).
- ³³ K. Wiesenfeld, S. P. Benz, and P. A. A. Booi. J. Appl. Phys. **76**, 3835 (1994).
- ³⁴ K. Wiesenfeld, A. S. Landsberg, and G. Filatrella. Phys. Lett. A **233**, 373 (1997).
- ³⁵ Similar effects have been discussed by W. A. Al-Saidi and D. Stroud, Phys. Rev. **B65**, 224512 (2002).

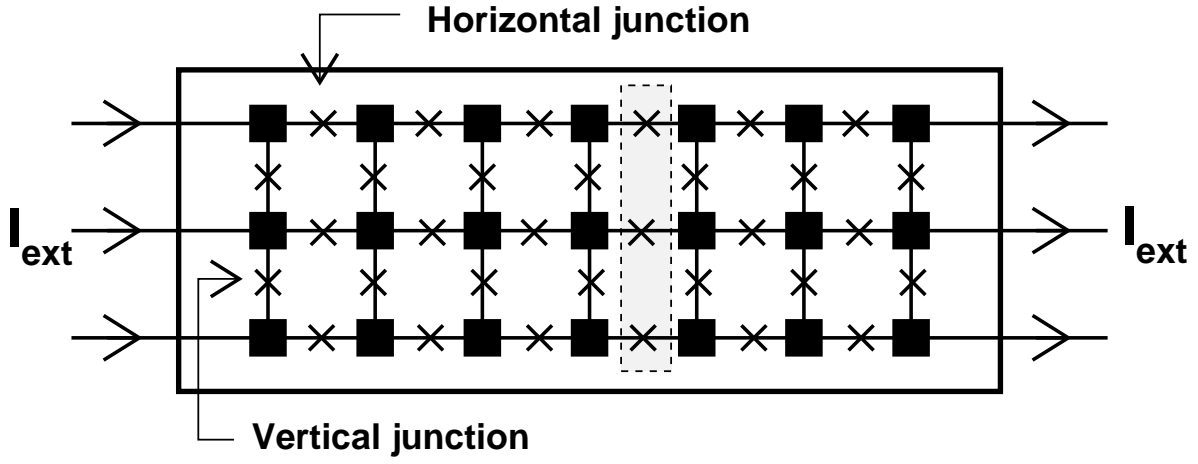


FIG. 1: Sketch of the array geometry in our model. There are $(M \times N)$ superconducting islands (black squares), making $[(M - 1) \times N + (N - 1) \times M]$ Josephson junctions (crosses). An external current I^{ext} is injected into each junction at one end of the array and extracted from each junction at the other end. The array is placed in an electromagnetic cavity which supports a single resonant photon mode of frequency Ω . The dashes denote a “row” of junctions, which is perpendicular to the current bias and is comprised of horizontal junctions.

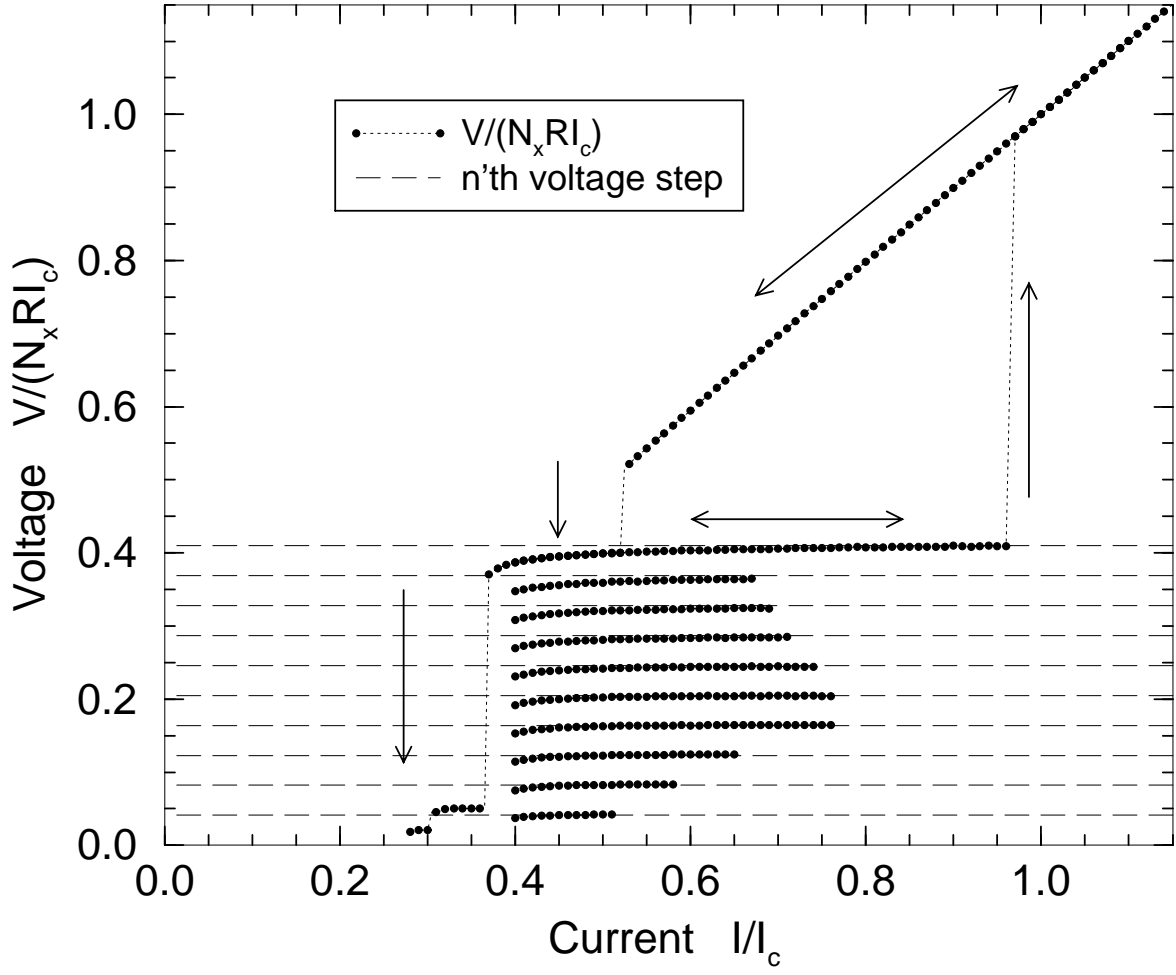


FIG. 2: Calculated current-voltage characteristic for a 10×4 array with cavity frequency $\tilde{\Omega} = 0.41$, capacitance parameters $\beta_c = 20$ and $\beta_d = 0.05$, disorder parameter $\Delta = 0.05$ and junction-cavity coupling in the horizontal direction $\tilde{g}_x = 0.012$. The horizontal dashed lines show expected voltages for the various SIRS's. These correspond to different numbers of rows of horizontal junctions in the active state. Arrows denote that the given IV was taken for increasing or decreasing current.

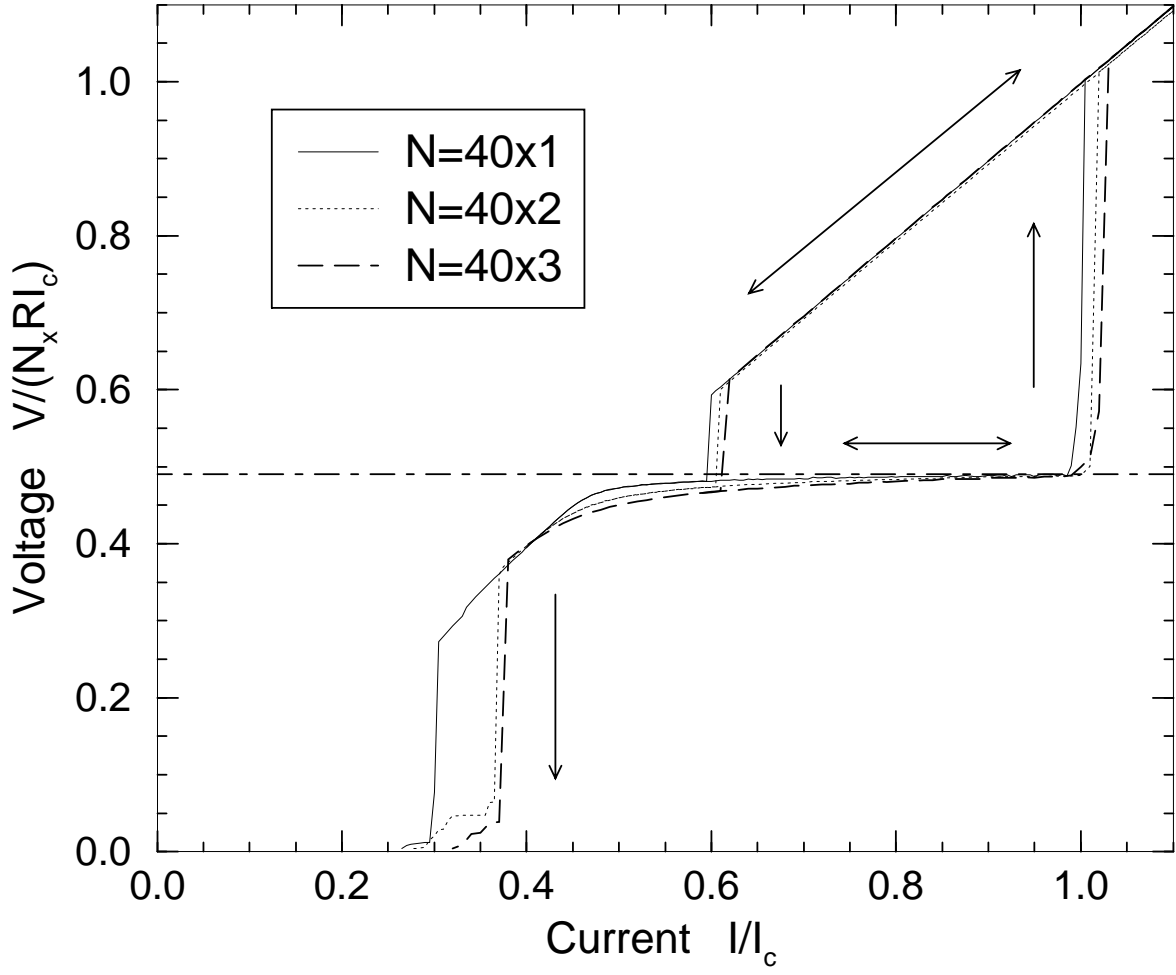


FIG. 3: Calculated current-voltage characteristics for a 40×1 (full line), a 40×2 (dotted line) and a 40×3 (long-dashed line) array, all with $\tilde{g}_x = 0.015$, $\tilde{\Omega} = 0.49$, $\beta_c = 20$, $\beta_d = 0.05$ and $\Delta = 0.05$. The horizontal dot-dashed line shows the expected SIRS position. Note that as the array width increases, the smallest \tilde{I} at which all the active junctions phase-lock on the SIRS also increases. Hence, increasing the array width and increasing \tilde{g}_x have a similar effect.

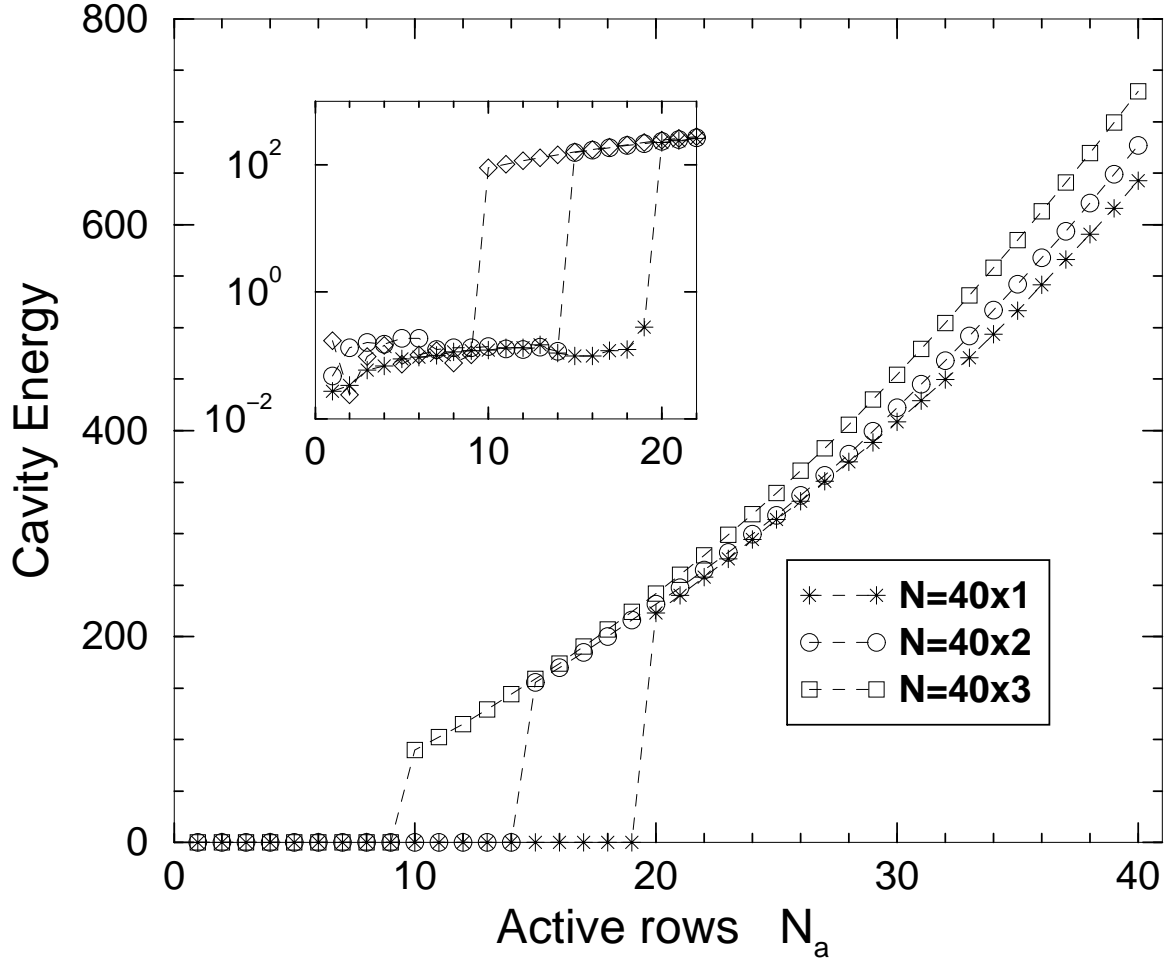


FIG. 4: Time-averaged scaled energy \tilde{E} in the resonant cavity as function of active number of rows for a 40×1 (asterisks), a 40×2 (circles) and a 40×3 (squares) array with driving current $\tilde{I} = 0.58$. All the other parameters are the same as those of Fig. 3. Inset: an enlargement of the IV characteristics near the synchronization threshold, on a logarithmic vertical scale. The threshold number of active junctions for synchronization decreases with increasing array width.

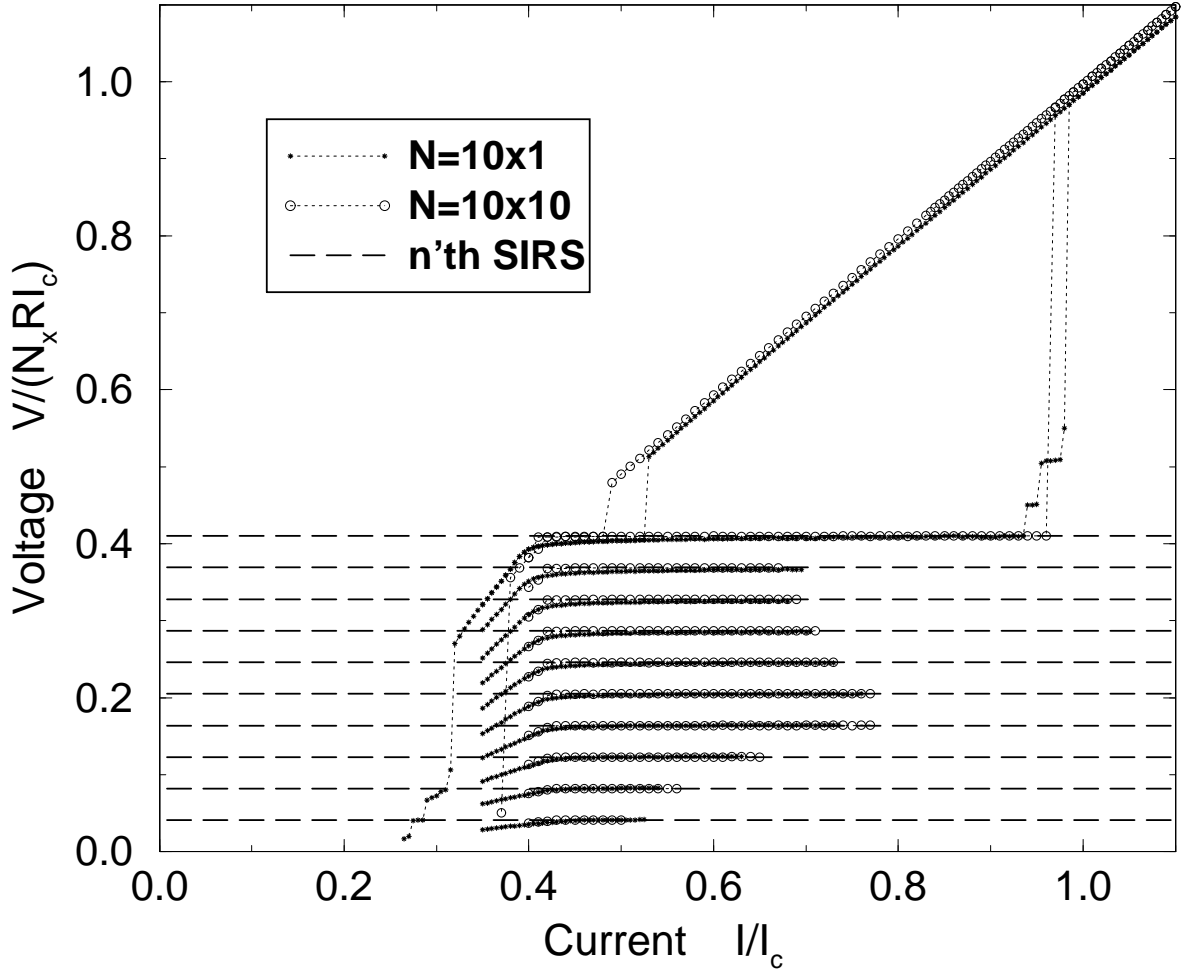


FIG. 5: IV characteristics for a 10×1 array (*) and a 10×10 array (o). The 10×1 array has parameters $\tilde{g}_{x,10 \times 1} = 0.0259$, $\tilde{\Omega} = 0.41$, $\beta_c = 20$, $\beta_d = 0.05$ and $\Delta = 0.05$. The expected SIRS positions of the SIRS's are marked by horizontal dashed lines. The 10×10 array has $\tilde{g}_{x,10 \times 10} = 0.00259$, and the other parameters are the same as for the 10×1 array. The IV characteristics are shown for both increasing and decreasing current drive.

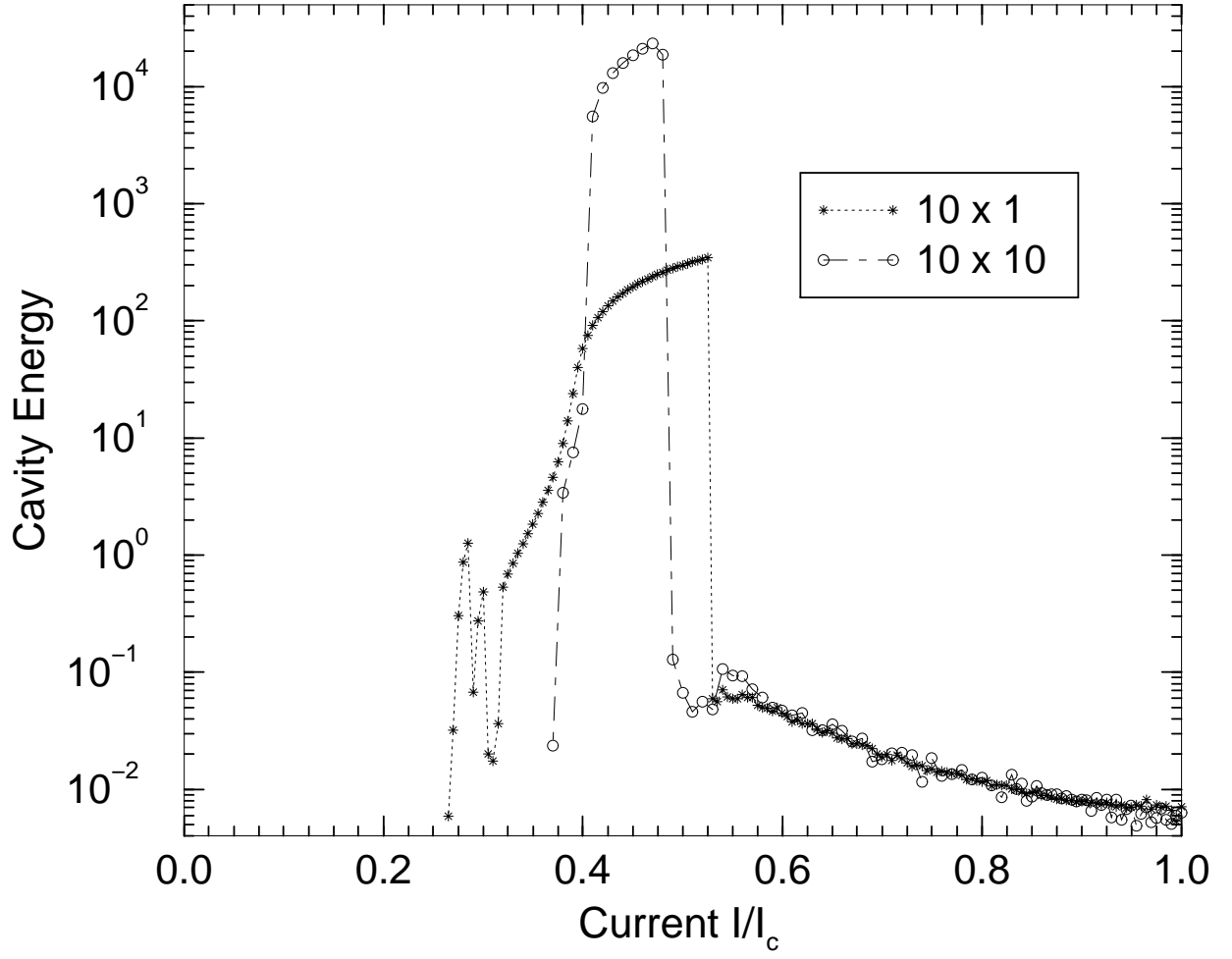


FIG. 6: Time-averaged reduced cavity energy \tilde{E} , for a 10×1 array and a 10×10 array for the same choice of array parameters as in Fig. 5. The calculations are carried out on the decreasing current branch with all rows active. \tilde{g}_x for the 10×10 array is 10 times smaller than that of the 10×1 array.